This is the accepted manuscript made available via CHORUS. The article has been published as:

Topology and self-assembly of defect-colloidal superstructure in confined chiral nematic liquid crystals

M. B. Pandey, P. J. Ackerman, A. Burkart, T. Porenta, S. Žumer, and Ivan I. Smalyukh

Phys. Rev. E **91**, 012501 — Published 5 January 2015

DOI: 10.1103/PhysRevE.91.012501

Topology and Self-Assembly of Defect-Colloidal Superstructure in Confined Chiral Nematic Liquid Crystals

M.B. Pandey,[1] P.J. Ackerman,[1,2] A. Burkart,[1] T. Porenta,[3] S. Žumer,[3,4] and Ivan I. Smalyukh[1,5,6*]

[1]Department of Physics, University of Colorado, Boulder, CO 80309, USA

[2]Department of Electrical, Computer, and Energy Engineering, University of Colorado, Boulder, CO 80309, USA

[3]Faculty of Mathematics and Physics, University of Ljubljana, Jadranska 19, 1000 Ljubljana, Slovenia.

[4]J. Stefan Institute, Jamova 39, 1000 Ljubljana, Slovenia.

[5]Liquid Crystal Materials Research Center and Materials Science and Engineering Program, University of Colorado, Boulder, CO 80309, USA

[6]Renewable and Sustainable Energy Institute, National Renewable Energy Laboratory and University of Colorado, Boulder, CO 80309, USA

[*]E-mail: ivan.smalyukh@colorado.edu

We describe formation of defect-colloidal superstructures induced by microspheres with normal surface anchoring dispersed in chiral nematic liquid crystals in confinement-unwound homeotropic cells. Using three-dimensional nonlinear optical imaging of director field, we demonstrate that some of the induced defects have nonsingular solitonic nature while other are singular point and line topological defects. The common director structures induced by individual microspheres have dipolar symmetry. These topological dipoles are formed by the particle and a hyperbolic point defect (or small disclination loop) of elementary hedgehog charge opposite to that of a sphere with perpendicular boundary conditions, which in cells with thickness over equilibrium cholesteric pitch ratio approaching unity are additionally interspaced by a looped double twist cylinder of continuous director deformations. The long-range elastic interactions are probed by holographic optical tweezers and videomicroscopy, providing insights to the physical underpinnings behind self-assembled colloidal structures entangled by twisted solitons. Computer-simulated field and defect configurations induced by the colloidal particles and their assemblies, which are obtained by numerically minimizing the Landau de Gennes free energy, are in agreement with the experimental findings.

1. Introduction

Nematic liquid crystals give rise to novel elastic colloidal interactions [1] and are promising fluid host media for reconfigurable self-assembly of nano- and micro-sized colloidal particles [2-22], as well as for exploiting fundamental and applied aspects of colloidal dynamics [23-25]. Colloidal inclusions induce elastic distortions [1] in the long-range molecular alignment of the liquid crystal medium and then interact with each other via elasticity-mediated interactions to minimize elastic energy due to these distortions [26]. An interesting open question is the role of chirality in guiding such elastic interactions and the ensuing self-assembly of particles. Similar to chiral magnets [27-29], chiral nematic liquid crystals (CNLCs) are capable of hosting stable nonsingular topologically nontrivial particlelike solitonic field configurations in the molecular alignment field, i.e. in the director field $\mathbf{n}(\mathbf{r})$ describing patterns of long molecular axis orientation in these calamitic nematic systems [30-37]. These twisted solitonic director structures include both two-dimensional (2D) skyrmions in the form of double-twisted tubes of $\mathbf{n}(\mathbf{r})$, also called "baby skyrmions" [33], and three-dimensional skyrmions, such as torons and hopfions comprising double twist tori, i.e. closed loops of double-twist cylinders of $\mathbf{n}(\mathbf{r})$ [34,35]. Given that the nematic ground state manifold $\mathbf{R}P^2$ is a sphere with all antipodal points identified [36], these 2D and 3D skyrmions are labeled by elements of the second and third homotopy groups, $\pi_2(\mathbf{R}P^2)=\mathbf{Z}$, and $\pi_3(\mathbf{R}P^2)=\mathbf{Z}$, respectively [35-37]. They have been experimentally realized in confinement-unwound CNLC cells with perpendicular surface boundary conditions and cell thickness comparable to the equilibrium cholesteric pitch [34, 35,37], the distance over which $\mathbf{n}(\mathbf{r})$ in the ground state CNLC twists around the helical axis by 2π. Since the transition from uniform to solitonic $\mathbf{n}(\mathbf{r})$ of the skyrmions is discontinuous in nature, the common approaches of generating such solitons involve focused laser beams [33-35], phase transitions [33], and hydrodynamic instabilities [33], which can transform the initial confinement-unwound homeotropic director field to that with individual solitons or their arrays. Recent studies of cholesterics confined to a thin layer, where homeotropic surface boundary conditions stabilize unwound homogenous director field, indicated that colloidal microspheres with tangential surface boundary conditions can lead to stable or metastable 3D and 2D skyrmionic solitons [37]. The individual particles are dressed and multiple particles are entangled by the looped double-twist cylinders of $\mathbf{n}(\mathbf{r})$ occurring to minimize the overall free energy of the constrained CNLC [33]. This resulted in the formation of unusual field and defect configurations around individual colloidal particles and unusual forms of their self-assembly [37].

In this work, we demonstrate that colloidal microspheres with perpendicular (homeotropic) surface boundary conditions can also give rise to skyrmionic structures. As they are complements to point defects and loops that always accompany homeotropic colloidal particles, they greatly enrich the host of defect and field configurations found in such colloidal systems [1-26, 37]. Using a combination of 3D imaging and non-contact optical manipulation [38], combined with numerical modeling based on minimization of the Landau-de Gennes free energy of confined CNLCs [37, 39], we reveal that microspheres with perpendicular anchoring dispersed in unwound CNLCs can induce not only hyperbolic point defects and closed half-integer line defect loops [1, 26] ranging from a simple Saturn ring to nematic braids, as in the case of nonchiral nematics, but also a large number of solitonic nonsingular and mixed singular-nonsingular particle-localized field configurations [37]. In our structural study, the CNLC colloidal dispersions are examined under a microscope and, simultaneously, colloidal interactions are probed using holographic optical tweezers [37]. The particles are moved closer or farther away from each other to set the initial conditions. Once the laser is turned off, motion of the particles is recorded using video microscopy and center-to-center colloidal separation versus time data are extracted using particle-tracking software. From these data, we estimate elastic forces and interaction potentials. The quantitative analysis of the inter-particle colloidal interactions mediated by elasticity and sharing of defects between multiple particles that we report in this work provides insights into physical underpinnings behind the unusual and diverse forms of their self-assembly.

2. Materials and Techniques

2.1. Sample preparation

To prepare cells, glass plates were washed with Alconox detergent in a supersonic bath for two hours and then rinsed with deionized water, acetone, and isopropyl. They were then treated for homeotropic surface boundary conditions in one of the following three different ways, which all yield similar results in terms of colloidal interactions and self-assembly, indicating that our findings are general and not dependent on selection of alignment materials. The glass plates were treated by means of dip-coating in a 1wt.% aqueous solution of N,N-dimethyl-n-octadecyl-3-aminopropyltrimethoxysilyl chloride (DMOAP), imposing perpendicular surface boundary conditions for **n** [11]. Alternatively, two kinds of polyamide coatings were used separately for the homeotropic surface treatment, SE-1211 and SE-5661 (both obtained from AlphaMicron, Inc.), allowing us to assure that the reported self-assembly behavior is not limited to specific alignment layers. In some cases, the polyamides were mixed with plastic microparticles and then coated on the glass plates to study induced defects due to such surface-bound particles and interaction between them and mobile particles in the CNLC bulk. The glass plates were spincoated with the polyamide or with the polyamide-spacer mixture using a G3P-8 Spin Coater (from Specialty Coating Systems). After spin coating, the slides were baked at 100 °C for approximately an hour to promote crosslinking and formation of robust homeotropic alignment films. CNLC cells with cell gap thicknesses such as d = 6, 7, 10, 15, 18, 24 and 30 μm were produced by sandwiching parallel glass substrates interspaced by glass fiber segments or spherical plastic spacers of corresponding diameters.

We have prepared the CNLC by doping a chiral additive S-811 (also referred to as ZLI-811, from EM Chemicals) into commercial nematic mixtures AMLC-0010 and E-31, which were obtained from Alphamicron, Inc and EM Chemicals, respectively, and used as supplied. The value of the pitch $p = 1/(h_{HTP} \times C_{chiral})$ of the CNLC of interest was varied by choosing an appropriate concentration C_{chiral} of the chiral dopant in the nematic host for the known values of the so-called "helical twisting power" h_{HTP} taken from literature (e.g. h_{HTP} =10.47μm^{-1} for S-811 in the AMLC-0010) [40]). The birefringence of AMLC-0010 is $\Delta n = 0.078$ and the elastic constants describing the splay, twist, and bend deformations of the director in AMLC-0010 are K_{11} = 17.2pN, K_{22} = 7.51pN, K_{33} = 17.9pN, respectively [40]. We used silica microspheres of diameters 3 μm and 4 μm, which were surface-functionalized with DMOAP to impose homeotropic surface boundary conditions on the LC director **n** [11]. Alternatively, we also used 6 μm plastic particles of two different kinds which tended to distort the nematic liquid crystal director in aligned cells more or less strongly due to imposing, respectively, relatively strong and weak perpendicular anchoring on their surfaces. The mixture of the CNLC and microspheres was sonicated for 10h to get uniform distribution of colloidal particles. CNLC colloidal dispersions were then introduced into a cell of thickness *d* smaller or equal to *p* by capillary forces and then sealed with epoxy.

2.2. Optical imaging and manipulation

The CNLC colloidal dispersions are probed using a polarizing optical microscope (POM), three-photon excitation fluorescence polarizing microscopy (3PEF-PM), and holographic optical tweezers (HOT) [38]. Motion of the particles was studied using video microscopy [11]. Movies recorded at 15 frames per second rates were converted into image sequences and analyzed in ImageJ software (from NIH). The center-to-center colloidal separation-versus-time data were extracted with precision of 5-10nm and then utilized to calculate velocities and forces. Since inertia effects are negligible because the particle motion is highly overdamped, the elastic interaction forces were determined from their balance with the effective viscous drag force calculated using the Stokes Law [41], $F = 6\pi\eta R dr/dt = \zeta dr/dt$, where R is the radius of the particles, η is the viscosity of the liquid crystal, and dr/dt is the velocity of a particle.

The integrated setup of HOT and 3PEF-PM was built around an inverted microscope IX-81 (Olympus). The imaging was performed using oil-immersion 100x and 60x objectives with a numerical aperture of 1.4 [38]. The use of low-birefringence AMLC-0010 [40] allowed us to mitigate common artifacts related to 3D imaging of twisted and chiral structures, including the ones associated with the so-called Mauguin effect of imaging light's polarization following the twist of director as light propagates along the helical axis [38]. HOT utilized a phase-only spatial light modulator (from Boulder Nonlinear Systems) and an Ytterbium-doped fiber laser (from IPG Photonics) operating at 1,064 nm [38]. 3PEF-PM imaging employed a tunable Ti-Sapphire oscillator (680-1,080 nm tuning range, obtained from Coherent) emitting 140 fs pulses at a repetition rate of 80 MHz and a photomultiplier tube detector H5784-20 (obtained from Hamamatsu) [38]. The fluorescence emission (collected within a 60nm spectral range using a band-pass optical filter with the central wavelength at 417 nm) was a result of three photon absorption due to excitation of the LC and chiral agent molecules at 870nm, as discussed in details elsewhere [37, 38]. Optical resolution of the 3PEF-PM imaging is on the order of 300-500nm [38]. Due to the nonlinear optical nature and also since the transition dipole moments of multiphoton absorption and fluorescence orient along the director, the strong ($\propto \cos^6\theta$) dependence of the 3PEF-PM fluorescence on the angle θ between $\mathbf{n}(\mathbf{r})$ and the linear polarization of excitation light allows for reconstruction of complex three-dimensional director fields around the studied colloidal particles. The maximum-intensity areas in the fluorescence textures correspond to the regions where linear polarization of the laser excitation light is parallel to anisotropic LC molecules and $\mathbf{n}(\mathbf{r})$ [38]. The dark areas with minimum fluorescence correspond to polarization of excitation light perpendicular to $\mathbf{n}(\mathbf{r})$. We also obtain 3PEF-PM images with circularly polarized excitation, which depict the 3D spatial pattern of sample regions with $\mathbf{n}(\mathbf{r})$ tilted away from the optical axis of the microscope and the cell normal [34, 37].

2.3. Theoretical modeling

Numerical modeling is based on the minimization of the free energy by phenomenologically combining Landau-de Gennes free energy terms describing CNLC elasticity and variable nematic degree of order and the surface anchoring energy into a free energy functional using an order parameter tensor Q_{ij} [37, 39, 41]. This modeling allows for characterization of minimum-energy $\mathbf{n}(\mathbf{r})$ and spatial changes in the degree of order in the vicinity of colloidal microspheres [37]. Minimization of the free energy is performed numerically for perpendicular boundary conditions using explicit finite difference scheme on a cubic mesh and material and cell parameters corresponding to the experiments [39]. Strong polar surface anchoring coefficient of 10^{-3} Jm^{-2} and moderate cholesteric confinement ratio of $d/p \sim 0.8$ were used in the computer simulations. The numerical minimization of free energy yields stable or metastable $\mathbf{n}(\mathbf{r})$ that is subsequently used to visualize structures and computer-simulate 3PEF-PM textures [37-

39], allowing for a direct comparison of theoretical predictions and experimental findings. These simulations are performed while disregarding the finite resolution effects as well as assuming that the polarization changes in the thin films of the low-birefringence CNLC can be neglected.

3. Results

3.1. Field and defect configurations induced by individual colloidal particles

Perpendicular boundary conditions on particle surfaces cause elastic distortions of the director field and defects that match them to the uniform far-field director. In addition to the strength of the polar surface anchoring on particle surfaces (which in so far studied physical systems is in the value range of 10^{-3}-10^{-6} J/m^2 [40] and cannot be tuned or reduced to zero), the **n**(**r**)-structure formed around the colloidal beads is dependent on the thickness of the cell d and equilibrium cholesteric pitch p of the CNLC material; note that there would be no particle-induced structures if the surface anchoring were to be progressively reduced to zero. For constrained cholesterics with $d/p<0.60$ and particles of diameter $2R$ much smaller than d and p, where R is the microspehere radius, we observe the usual nematic defect-colloidal dipoles (Fig. 1a-c) formed by a microsphere with perpendicular anchoring and a hyperbolic point defect nearby. Although a chiral additive is present in the nematic colloidal system, the strong normal boundary condition at the confining glass plates of the cell force the uniform director field far away from the particles and the induced **n**(**r**) around the particles is similar to that in dipolar configurations of non-chiral nematic colloidal systems. 3D imaging is consistent with the analytical model of the director field of non-chiral nematic colloidal dipoles shown in Fig. 1d-f [26]. 3PEF-PM images shown in Fig. 1d,e reveal that the defect-colloidal structures can be elastic dipoles pointing up or down, similar to the elastic dipoles in nonchiral nematics. This 3D imaging also reveals that, similar to nonchiral nematics [1, 26], the hyperbolic defect is at a relatively short distance from the particle surface, within $(1.1$-$1.25)R$ from the particle center.

In the CNLC cells with d/p ratios within ~0.75-0.95, we observe that larger particles with size $2R=(0.1$-$1)d$ spontaneously appear to be “dressed” by well-defined twisted solitonic director configurations. The microspheres are accompanied by the localized doughnut-shaped birefringent **n**(**r**)-structures (Fig. 2a). The small dark brushes in bright doughnut-shaped birefringent rings (Fig. 2a) around particles have spiraling directions dependent on whether the point defects reside above or below the beads, as we reveal using the polarized 3D imaging (in-plane views Fig. 2b-d and side views Fig. 2e-j). These particles levitate at two different depth levels, below (Fig. 2 e,f,h) and above (Fig. 2 g,i,j) the cell's midplane. Although the details of director configurations vary with changing *d*/*R* and *d*/*p*, they are all found to be homeomorphic to each other. Similar to dipolar structures in nonchiral nematics, they always contain a singular defect in a form of a hyperbolic point defect or a small defect loop (Fig. 2k), but additionally also a nonsingular soliton in a form of a closed loop of a double-twist tube of **n**(**r**) interspacing the particle and the singular defect. Interestingly, depending on *d*/*p* and *d*/*R*, the distance between particle's center and the singular defect varies from ~1.2*R* to ~7*R*, as revealed by experimental 3PEF-PM vertical cross-sectional micrographs (Fig. 2e-j) matching the ones obtained by means of numerical modeling performed for different sizes of the particle relative to *d* (Fig. 2k,l and Fig. 3). The looped double-twist cylinder, an inherent part of the studied structures, is typically somewhat stretched along the depth of the sample (Figs. 2k and 3b) in case of weak confinement and compressed in case of stronger confinement (Fig.3d). The director field is continuously deformed through additional elastic distortions to match the perpendicular boundary conditions on the particle surface and at confining substrates, along with the uniform vertical far-field director. In the intermediate range of *d*/*p* ≈ 0.6-0.75, the conventional director configurations with the hyperbolic point defect alone (Fig. 1), which are found on some of the particles, are observed to co-exist with the new types of director configurations induced by other particles (Fig. 2). Focusing of the laser beam of power 30mW and higher beneath or above the colloidal particles allows one to induce structural transformations between the two species of dipoles and corresponding particle-induced distortions and defects, which is similar to what we previously observed for particles with tangential surface anchoring [37].

3.2. Pair interactions and self-assembly of elastic dipoles and the corresponding director field configurations

By releasing colloidal particles decorated by solitons at different center-to-center separations using optical manipulation, we reveal that particles with parallel elastic dipoles pointing upwards or downwards interact repulsively at all center-to-center distances ranging up to 8-10 particle diameters. On the other hand, particles with dipoles pointing in opposite direction tend to attract when center-to-center distance between them is ≤5R, forming colloidal dimers, similar to nematic dipolar colloids (Fig. 4). Interaction between two individual particles is highly selective in such a way that it always leads to self-assemblies with alternating depth location of the particles and anti-parallel elastic dipole orientations. This formation of self-assemblies is similar to the behavior of microspheres with tangential surface boundary conditions in similarly unwound CNLC cells [37]. POM (Fig. 4a) and 3PEF-PM (Fig. 4c-f) textures have low symmetry, being different from the dipolar dimers in nonchiral nematics. However, the 3PEF-PM textures of the dipolar assemblies (Fig. 4d,f) obtained for circularly polarized excitation light show qualitative resemblance to the textures we previously reported for particles with tangential boundary condition in similar dimer-type assemblies [37], although the **n**(**r**) orientation at particle surfaces differs by 90 degrees due to the perpendicular boundary conditions. Interestingly, similar to the case of particles enforcing planar surface anchoring, the studied homeotropic CNLC colloids do not preserve their original axially symmetric structure upon self-assembly (Fig. 4). These colloidal dimers are formed by pairs of antiparallel elastic dipoles that become entangled by low-symmetry solitonic twisted **n**(**r**) in-between and around them upon self-assembly, as revealed by 3D imaging (Fig. 4) and confirmed by numerical modeling (Fig. 5).

In addition to dimers, larger colloidal assemblies can form too (Fig. 6). In these larger assemblies, elastic interactions also lead to alternating depth location and elastic dipole orientation. Brightfield and cross-sectional 3PEF-PM images (Fig. 6) reveal that the alternating elastic dipole orientation is a guiding principle of this self-assembly and characteristic also of soliton-dressed colloidal trimers, tetramers, as well as longer chains and other assemblies, qualitatively similar to the behavior of colloidal particles with tangential anchoring dressed with twisted solitons that we studied previously [37].

The inter-particle colloidal interaction between the elastic dipoles and the ensuing colloidal self-assembly are further investigated with the use of holographic optical tweezers and videomicroscopy (Fig. 7). When the particles are released at different initial separations, we find that oppositely oriented colloidal dipoles in an unwound CNLC attract each other (Fig. 7a) while parallel dipoles always repel from each other (Fig. 7b), similar to nematic dipolar colloids. This behavior is enriched when dipoles are dressed by double twist solitons (Fig. 2), which often leads to a "screening" (weakening) of the dipole moments, similar to the case of particles with tangential surface anchoring dispersed in unwound CNLCs [37]. The screening partially resembles the effect observed in the case of colloidal particles in bulk cholesterics [42]. Assuming a balance of the elastic interaction force with the viscous drag force and using the data shown in Fig 7a,b as well as a viscous drag coefficient determined through characterization of Brownian motion [37], we find the maximum absolute values of pair-interaction force ~6-8 pN and also estimate the maximum interaction energy (the so-called "binding energy") of the order of 8,000 k_BT.

The strength of interactions is dependent on the strength of surface anchoring on the particles. For example, plastic microspheres with 2R=6μm of the type that impose strong perpendicular boundary conditions for $\mathbf{n}(\mathbf{r})$ repel from each other up to distances of ≈29μm when forming parallel elastic dipoles in unwound CNLC cells with p=20μm and d=15μm. Under the same conditions, the plastic particles of the same size 2R=6μm but with weaker homeotropic surface anchoring repel only up to distances of ∼11 μm. This is consistent with somewhat smaller spatial extent of elastic distortions around the plastic beads with weak anchoring as compared to the ones with strong surface anchoring, which results in both attractive and repulsive forces and potentials weaker by a factor of 2-3 as compared to the particles with strong surface anchoring. Qualitatively, this can be ascribed to the weaker homeotropic surface anchoring allowing the double-twist cylinder to exist closer to the bead, since the director at particle's surface can deviate from the easy axis and thus match more closely the field configuration of the looped double twist cylinder encircling it. Interestingly, the strength of interactions between a surface-attached and a mobile particles is slightly weaker but of the same order of magnitude as interactions between such particles when they are both mobile in the unwound CNLC layer. For example, surface-attached and mobile elastic dipoles formed by plastic microspheres repel up to distances of ≈16μm, which is smaller from the ≈29μm repulsion distance of two similar mobile particles under otherwise the same conditions, an effect that can be explained by surface screening of elastic distortions. This is consistent with our observations that surface-attached particles with homeotropic boundary conditions also induce looped double-twist cylinders, similar to the colloidal particles undergoing Brownian motion in the unwound CNLC layer.

3.3. Structural diversity of colloidal self-assemblies

One of the characteristic features of CNLC confined in homeotropic cells with $d/p\sim1$ is that a large number of nonsingular solitonic structures and singular defects can co-exist (or appear under similar conditions) as stable or long-lived metastable states including torons, hopfions, fingers, baby skyrmions, etc. [33-35, 37, 44]. This structural diversity is also characteristic of multi-particle colloidal assemblies in our confinement-unwound CNLC colloidal system (Figs. 8 and 9). While the common feature is that particles in the colloidal self-assemblies are encircled or entangled by different double-twist-cylinder solitons, the details of how this happens are dependent on the particle size relative to d and p, the strength of surface anchoring, etc. However, even identical particles in the same CNLC cell can exhibit a large structural diversity of field configurations while forming various dimers, trimers, tetramers, and larger assemblies (Figs. 8 and 9). For example, by melting the different sample regions using high-power laser tweezers (~200mW) and than having these regions relax back to a stable or metastable states at no fields, one observes that particles typically reassemble in structures with different $\mathbf{n}(\mathbf{r})$ configuration (Figs. 8 and 9). In addition to the nonsingular solitonic structures in the form of double-twist tubes (typically closed or terminating on the particles), one can also identify singular point and line defects. For example, the structures of $\mathbf{n}(\mathbf{r})$ around dimers formed by both silica (Fig. 9a-f) and plastic beads (Fig. 8a-f) are often different from the stable configuration observed most frequently in experiments (Fig. 4) and also obtained through the numerical modeling (Fig. 5). Rather than having point defects or small disclination rings above and below the particles, as in monomers or in the most commonly observed dimers (Fig. 5), some of the particles within the self-assembled dimer configurations appear to share single singular disclination loops in-between them, as also observed in the numerical models presented in Fig. 10. Interestingly, the POM and 3PEF-PM textures (Fig. 10c,d) indicate that the main changes in **n**(**r**) occur in-between the particles and distortions away from the particles resemble the textures simulated/imaged for the ground-state configuration (Fig. 4d and Fig. 5). This is consistent with the results of modeling and suggests that the closed disclination loops in Fig. 10 have replaced the two hyperbolic point defects seen in Fig. 5, resulting in a topologically similar structure.

Even larger diversity of director and defect structures is observed as the number of particles in the self-assemblies is increased beyond two, as seen from the examples of colloidal trimers (Figs. 8,9, 11, and 12). Computer simulations, similar to the case of dimers, reveal that as the cell and material parameters are varied, some of the point defects within the colloidal dipoles (Fig. 11a,b) or all of them (Fig. 11c,d) are often replaced by complex-shaped disclination loops, while these particles are still surrounded by double-twist-cylinder-like solitonic structures similar to the ones observed experimentally (Figs. 8 and 9). Although our experiments where performed only for micrometer-sized particles, the computer simulations reveal that singular disclination loops are expected to be even more abundant as the thickness of the cell (*d*), particle size (2*R*), and cholesteric pitch (*p*) decrease to the submicron range (Fig. 12). These numerically simulated structures include single singular half-integer disclinations entangling all three particles in a trimer (Fig. 12a,b), as well as trimers with two or three disclinations that are shared by multiple particles or can be associated with individual particles (Fig. 12c-d).

The main reason for the long-term stability of various metastable and stable states is that they are separated by large energetic barriers and the interactions are associated with large binding energies (experimentally estimated to be of the order of 10,000 K_BT). Therefore, the particle assemblies can be easily entrapped in many different long-lived metastable states in addition to the ground state. In experiments, in addition to the closed loops of double-twist cylinder, we also observe fragments of the so-called cholesteric fingers of the first and second kinds [40, 43], which are “topologically neutral”, i.e. composed of self-compensating twist-escaped nonsingular disclination lines. They are observed in confined CNLC cells also without addition of colloidal particles, but the presence of the latter helps in their nucleation and stability (Figs. 8 and 9). For example, Fig. 9f shows a finger of the second kind (CF2) with two colloidal particles stabilized at a large distance from each other. The translationally invariant soliton-like structure of the CF2 embedding the particles makes the interaction between them very different from that in a homeotropic unwound CNLC, so that the particles do not attract or repel while being at a relatively large distance of several diameters from each other, which would be impossible in our frustrated cholesteric cells without their embedding into the cholesteric finger. The spacers commonly used for setting the cell thickness *d*, which were in the forms of 6μm plastic microspheres with relatively strong or weak surface anchoring and glass fiber segments of different diameters, also induce twisted solitonic structures similar to the ones observed around colloidal microspheres in the CNLC bulk (Fig. 8q, r), implying that the field configurations studied are rather common and emerge to relieve surface imposed frustration of unwound CNLC in homeotropic cells.

4. Discussion

Despite being found in the ground-state structures of all three cholesteric blue phases [45-49], double twist tubes are rarely observed in bulk cholesteric samples with the helicoidal ground state. The main reason is that, unlike for the blue phases, the benefit of realizing such solitonic field configuration due to the saddle-splay term of the free energy of a cholesteric LC is rather small relative to the cost of singular defects that need to accompany them to meet different surface boundary conditions in confined samples and topological constraints in the CNLC bulk, which is precisely the same reason as why blue phases with large lattice periodicity (larger than ~500nm) are unstable. In the frustrated CNLC cells, however, they can be generated and stabilized by various means in the forms of torons, hopfions, and 2D baby-skyrmions [33-35, 37]. Our study shows that colloidal particles, spacers, and other inclusions universally tend to stabilize the double twist cylinders, leading to formation of their closed loops around individual or multiple particles and spacers (Figs. 2 and 3) or their fragments terminating on different particles of multi-particle self-assemblies (Figs. 4-6 and 8-10). Since the net hedgehog charge of a looped double twist cylinder is zero [33, 37], the hyperbolic point defects (or small disclination loops of the same hedgehog charge ±1, with the relative sign dependent on the choice of direction of the decorating vector field [11]) compensate for the effective hedgehog charge of the radial director on the surface of the spherical particle [1, 11]. The topological charge conservation persists as the colloids form various self-assemblies embedded in the uniform unwound director field of the unwound CNLC, which again can be verified by vectorizing the director field lines and determining the hedgehog charges via mapping the director field around the defects onto the order parameter space.

Apart from providing an abundant source of $\pi_2(\mathbf{R}P^2)=\mathbf{Z}$ and $\pi_3(\mathbf{R}P^2)=\mathbf{Z}$ topological defects for fundamental studies [50], our finding that the loops of the double-twist cylinders appear also around the spacers setting CNLC cell thickness may impinge on the development of strategies for optimization of related technological applications, such as cholesteric guest-host devices based on CNLCs with negative dielectric anisotropy [40, 51, 52]. In these applications, it is important to maintain translationally invariant uniform or twisted configurations up to largest possible d/p values typically approaching unity [51, 52], which is important for optimizing absorption of unpolarized light by dichroic dyes, and also within a continuous range of applied voltages to assure a continuous light transmission control. Since the spacers are used to set the CNLC film thickness between glass or plastic substrates, they can partially contribute to degrading performance due to the appearance of the looped double-twist cylinders at no applied fields and their expansion/growth as the field is applied. The design of boundary conditions and the types of spacers is therefore important for optimizing performance of such CNLC-based dichroic guest-host devices.

5. Conclusions

To conclude, we have demonstrated spontaneous appearance of loops and curved fragments of double twist cylinders around individual homeotropic colloidal microspheres and their self-assemblies in confinement-frustrated homeotropic CNLC cells. Despite having dipolar symmetry, similar to elastic dipoles in nonchiral nematics, colloidal particles with homeotropic anchoring dispersed in the unwound CNLC at thickness/pitch ratios d/p=0.75-0.95 induce not only hyperbolic point defects but also loops of the double twist cylinders interspacing the particle and the point defect. Our findings demonstrate that chirality of the frustrated CNLC host has interesting consequences on the structure and self-assembly of colloidal structures as compared to non-chiral nematic counterparts through the stabilization of twisted solitonic structures in the forms of $\pi_2(\mathbf{R}P^2)=\mathbf{Z}$ and $\pi_3(\mathbf{R}P^2)=\mathbf{Z}$ nonsingular topological defects, in addition to other more common for liquid crystal colloids defects, also impinging on the self-assembled colloidal structures. Various colloidal inclusions may allow one to produce looped double twist cylinders of different lateral sizes relative to the intrinsic periodicity of the CNLC set by the equilibrium cholesteric pitch, potentially allowing one to forms hopfions and torons with different types of torus knots and Hopf indices [53]. In addition to their fundamental importance [50], the appearance of these solitonic twisted field configurations may also impinge on the optimization strategies in guest-host display and smart window applications [51, 52].

We acknowledge discussions with B. Senyuk, B. Taheri and Y. Yuan. This work was supported by the NSF Grant DMR-0847782 (M.B.P., A.B., P.J.A., I.I.S) and by the U.S. Department of Energy, Office of Basic Energy Sciences, Division of Materials Sciences and Engineering under Award ER46921, contract DE-SC0010305 with the University of Colorado (I.I.S.), as well as the Slovenian Research Agency grants No. P1-0099 and J1-2335 (T.P., S.Ž.). M.B.P. acknowledges support of the Indian Government through the DST-BOYSCAST Fellowship program.

References

[1] P. Poulin, H. Stark, T. C. Lubensky and D. A. Weitz, Science **275**, 1770 (1997).

[2] U. Tkalec, M. Škarabot, and I. Muševič, Soft Matter **4**, 2402 (2008).

[3] C. P. Lapointe, T. G. Mason, and I. I. Smalyukh, Science **326**, 1083 (2009).

[4] P. Poulin, V. Cabuil and D. A. Weitz, Phys. Rev. Lett. **79**, 4862 (1997).

[5] R. P. Trivedi, I. I. Klevets, B. Senyuk, T. Lee, and I. I. Smalyukh, Proc. Natl. Acad. Sci. U. S. A. **109**, 4744 (2012).

[6] F. Brochard, P. G de Gennes, J. Phys. (Paris) **31**, 691 (1970).

[7] B. I. Lev, S. B. Chernyshuk, P. M. Tomchuk, and H. Yokoyama, Phys. Rev. E **65**, 021709 (2002).

[8] P. Poulin and D. A. Weitz, Phys. Rev. E **57**, 626 (1998).

[9] D. Andrienko, M. P. Allen, G. Skačej and S. Žumer, Phys. Rev. E **65**, 041702 (2002).

[10] C. P. Lapointe, S. Hopkins, T. G. Mason, and I. I. Smalyukh, Phys. Rev. Lett. **105**, 178301 (2010).

[11] B. Senyuk, Q. Liu, S. He, R. D. Kamien, R. B. Kusner, T. C. Lubensky, and I. I. Smalyukh, Nature (London) **493**, 200 (2013).

[12] F. Mondiot, S. P. Chandran, O. Mondain-Monval, and J.-C. Loudet, Phys. Rev. Lett. **103**, 238303 (2009).

[13] J. Dontabhaktuni, M. Ravnik and S. Žumer, Soft Matter **8**, 1657 (2012).

[14] P. M. Phillips and A. D. Rey, Soft Matter **7**, 2052 (2011).

[15] G. M. Koenig, Jr., J. J. de Pablo, and N. L. Abbott, Langmuir **25**, 13318 (2009).

[16] G. M. Koenig, Jr., R. Ong, A. D. Cortes, J. A. Moreno-Razo, J. J. de Pablo, and N. L. Abbott, Nano Lett. **9**, 2794 (2009).

[17] A. V. Ryzhkova and I. Muševič, Phys. Rev. E **87**, 032501 (2013).

[18] M. Škarabot, M. Ravnik, S. Žumer, U. Tkalec, I. Poberaj, D. Babič, and I. Muševič, Phys. Rev. E **77**, 061706 (2008).

[19] B. Senyuk, J. S. Evans, P. J. Ackerman, T. Lee, P. Manna, L. Vigderman, E. R. Zubarev, J. van de Lagemaat, and I. I. Smalyukh, Nano Lett. **12**, 955 (2012).

[20] F. Mondiot, J.-C. Loudet, O. Mondain-Monval, P. Snabre, A. Vilquin, and A. Würger, Phys. Rev. E **86**, 010401(R) (2012).

[21] V. Tomar, T. F. Roberts, N. L. Abbott, J. P. Hernandez-Ortiz, and J. J. de Pablo, Langmuir **28**, 6124 (2012).

[22] D. Abras, G. Pranami, and N. L. Abbott, Soft Matter **8**, 2026 (2012).

[23] I. I. Smalyukh, A. V. Kachynski, A. N. Kuzmin, and P. N. Prasad, Proc. Natl. Acad. Sci. U.S.A. **103**, 18048 (2006).

[24] J. C. Loudet, P. Hanusse, and P. Poulin, Science **306**, 1525 (2004).

[25] A. Martinez, H. C. Mireles, and I. I. Smalyukh, Proc. Natl. Acad. Sci. U. S. A. **108**, 20891 (2011).

[26] T. C. Lubensky, D. Pettey, N. Currier, H. Stark, *Phys. Rev. E* **57**, 610 (1998).

[27] S. Muhlbauer et al., *Science* **323**, 915-919 (2009).

[28] N. Nagosa and Y. Tokura, *Nature Nanotech.* **8**, 899–911 (2013).

[29] U. K. Rößler, A. N. Bogdanov and C. Pfleiderer, *Nature* **442**, 797-801 (2006).

[30] J. Fukuda and S. Žumer, *Nature Communications* **2**, 246 (2011).

[31] A. N. Bogdanov, U. K. Rößler, and A. A. Shestakov, *Phys. Rev. E* **67**, 016602 (2003).

[32] A. N. Bogdanov and A. A. Shestakov, *Zh. Eksp. Teor. Fiz.* **113**, 1675–1697 (1998).

[33] P. J. Ackerman, R. P. Trivedi, B. Senyuk, J. van de Lagemaat, and I. I. Smalyukh. Phys Rev E 90, 012505 (2014)

[34] I.I. Smalyukh, Y. Lansac, N. Clark, and R. Trivedi. *Nature Mater.* **9**, 139-145 (2010).

[35] B. G. Chen, P. J. Ackerman, G. P. Alexander, R. D. Kamien, and I. I. Smalyukh, *Phys. Rev. Lett.* **110**, 237801 (2013).

[36] G.P. Alexander, B.G. Chen, E.A. Matsumoto, and R.D. Kamien. *Rev. Mod. Phys.* **84**, 497 (2012).

[37] M. B. Pandey, T. Porenta, J. Brewer, A. Burkart, S. Čopar, S. Žumer, and I. I. Smalyukh. Phys Rev E 89, 060502(R) (2014).

[38] R. P. Trivedi, T. Lee, K. A. Bertness, and I. I. Smalyukh. *Optics Express* **18**, 27658 (2010).

[39] S. Čopar, T. Porenta and S. Žumer. *Liquid Crystals* **40**, 1759 (2013).

[40] I.I. Smalyukh, B. I. Senyuk, P. Palffy-Muhoray, O. D. Lavrentovich, H. Huang, E. C. Gartland, Jr., V. H. Bodnar, T. Kosa, B. Taheri. Phys. Rev. E 72, 061707 (2005).

[41] P. M. Chaikin, T. C. Lubensky, *Principles of Condensed Matter Physics* (Cambridge Univ. Press, Cambridge, 2000).

[42] V. S. R. Jampani, M. Škarabot, S. Čopar, S. Žumer, and I. Muševič, *Phys. Rev. Lett.* **110**, 177801 (2013).

[43] P. Oswald, J. Baudry, and S. Pirkl, *Phys. Reports* **337**, 67-96 (2000).

[44] T. Porenta, S. Čopar, P. J. Ackerman, M. B. Padney, M. C. M. Varney, I. I. Smalyukh, and S. Žumer. *Sci. Rep.* **4**, 7337 (2014).

[45] R. M. Hornreich and S. Shtrikman, *Liq. Cryst.* **5**, 777-789 (1989).

[46] G. Heppke, B. Jéròme, H-S. Kitzerow, and P. Pieranski, *Liq. Cryst.* **5**, 813-828 (1989).

[47] R.M. Hornreich, M. Kugler, and S. Shtrikman, *J. de Physique* **46**, 47-60 (1985).

[48] P. Pieranski, P. E. Cladis, and R. Barbet-Massin, *J. Physique Lett.* **46**, L-973 - L-977 (1985).

[49] R.M. Hornreich, M. Kugler, and S. Shtrikman, *Phys. Rev. Lett.* **54**, 2099-2102 (1985).

[50] J. F. Sadoc and J. Charvolin. *J. Phys. A: Math. Theor.* **42**, 465209 (2009).

[51] B. Taheri, T. Kosa, V. Bodnar, *et al. Procs. SPIE* **7618**, 76180W (2010).

[52] B. Taheri, P. Palffy-Muhoray, T. Kosa, *et al. Procs. SPIE* **4021**, 114-119 (2000).

[53] P. J. Ackerman, J. van de Lagemaat, and I. I. Smalyukh. *Nat. Commun.* **5**, 6012, doi.1038/ncomms7012 (2014).

Figures

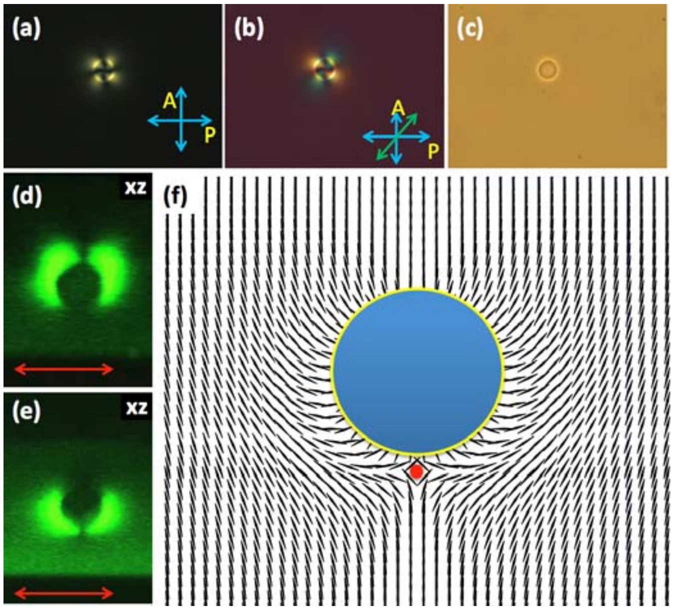

Fig. 1. Conventional colloidal elastic dipoles in CNLCs of equilibrium pitch p=33 μm prepared by doping a chiral additive S-811 into a nematic host AMLC-0010. (a-c) Optical micrographs of an unwound homeotropic cell with a 4 μm silica microsphere inducing an elastic dipole orthogonal to cell substrates obtained (a) between crossed polarizer (P) and

analyzer (A) marked by blue double arrows, (b) between the crossed polarizer and analyzer with an additional full-wave 530nm phase retardation plate having its slow axis marked by the green double arrow, and (c) without polarizers or other optical elements. (d, e) 3PEF-PM vertical xz cross-sections showing elastic dipoles with two opposite orientations and points defects (d) above and (e) beneath the beads. The cell thickness is visible from 3PEF-PM cross-sections relative to the 4 μm particle size. (f) The **n**(r)-configuration induced by a colloidal microsphere obtained using an anzats from Ref. [26], showing a good qualitative agreement with the experimental images depicted in (d,e) in hometropic confined cell; the hyperbolic bulk point defect is shown by a red filled circle.

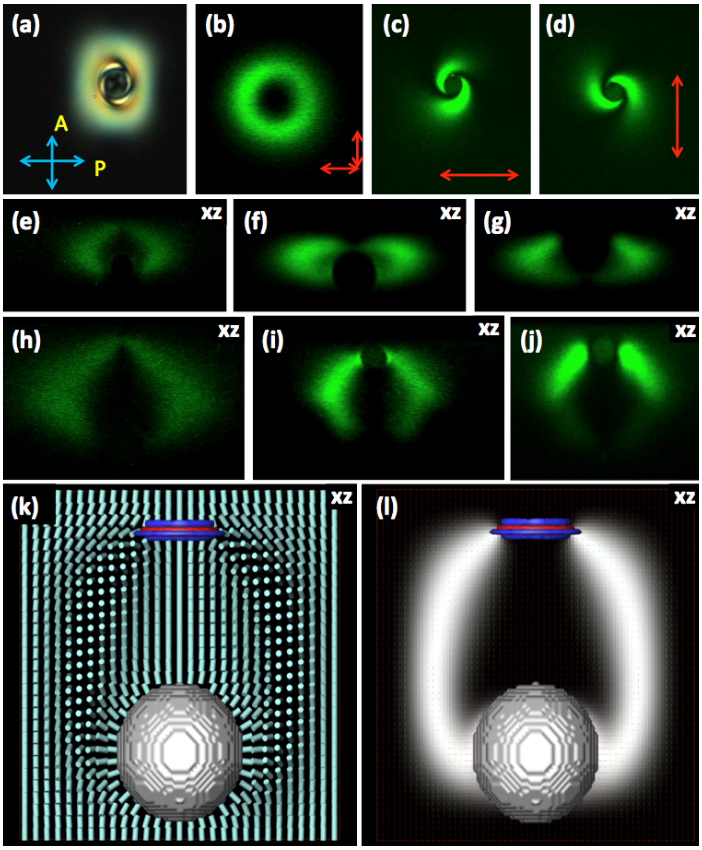

Fig. 2. CNLC colloidal dipoles with twisted solitons induced by 4μm silica spheres. (a) Polarizing optical micrograph (obtained between crossed polarizer and analyzer marked by blue arrows) showing a topological colloidal dipole in a homeotropic unwound CNLC cell of thickness $d \approx 10\mu m$ filled with a CNLCs of equilibrium pitch 10.6μm based on AMLC-0010 nematic host. (b-d) In-plane xy 3PEF-PM images of the colloidal dipole

obtained (b) for circularly polarized 3PEF-PM excitation light and (c,d) for two mutually orthogonal linear polarizations of 3PEF-PM excitation light (marked by red double arrows) in a cell of thickness *d*≈30 μm filled with a CNLCs of equilibrium pitch 33μm based on AMLC-0010 nematic host. (e-j) 3PEF-PM vertical xz cross-sections of the colloidal dipoles in cells of different thickness obtained for circularly polarized 3PEF-PM excitation light; the thickness is 10μm in (e), 7μm in (f,g), and 30μm in (h,i,j). (k) Computer-simulated **n**(r), depicted using cylinders, around a particle with hometropic anchoring; note that the small disclination loop above the particle is equivalent to a hyperbolic point effect. (l) The corresponding computer-simulated 3PEF-PM texture in the vertical plane for circular polarization of the 3PEF-PM excitation light.

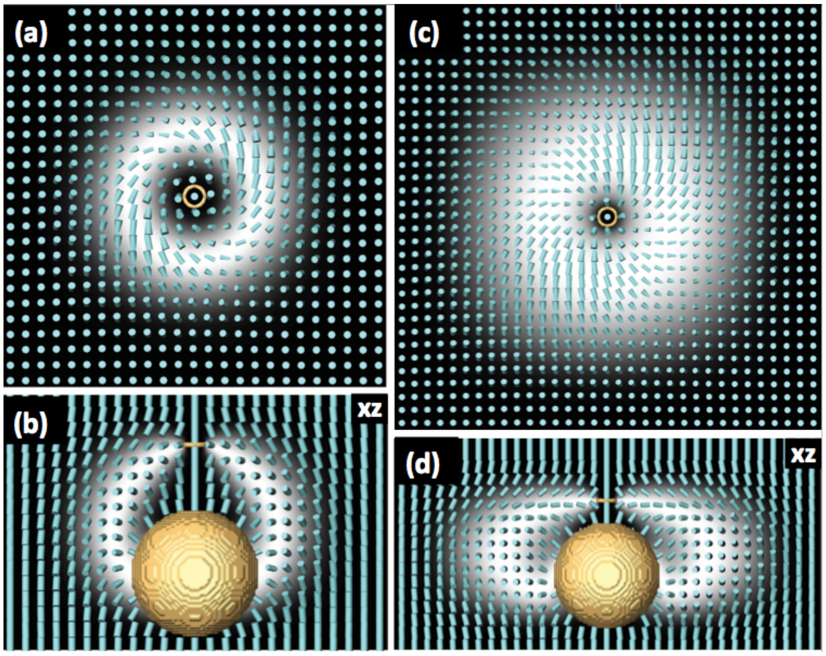

Fig. 3. Structures of skyrmion-decorated topological dipoles in CNLC cells. The spatial patterns of **n**(**r**) are depicted using cylinders and the small defect loops are presented by iso-surfaces of the reduced nematic order parameter [39]. (a-d) Co-located director structures (shown using cylinders) and 3PEF-PM images (grayscale intensity plots) shown in (a,c) in-plane (xy) cross-sections containing the singular defect loops and (b, d) corresponding vertical (xz) cross-sections of the CNLC cell for different ratios between the cell thickness *d* and the particle diameter 2*R*.

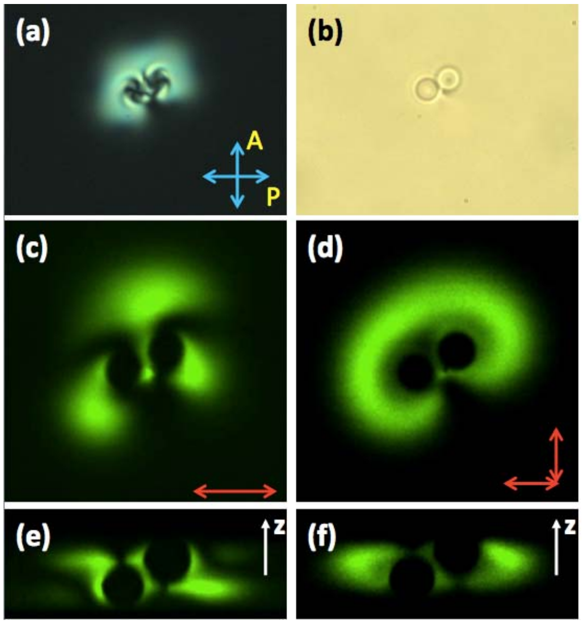

Fig. 4. Imaging of $\mathbf{n}(\mathbf{r})$ induced by colloidal dimers formed by two anti-parallel elastic dipoles induced by 4μm silica spheres in a cell of thickness $d \approx 7$μm filled with a CNLCs of pitch $p \approx 10.5$ μm prepared by doping a chiral additive S-811 in AMLC-0010 nematic host. (a) POM obtained between crossed polarizer and analyzer marked by blue arrows and (b) brightfield micrographs of a self-assembled dimer formed by two anti-parallel elastic dipoles. (c,d) In-plane and (e,f) vertical 3PEF-PM cross sections obtained for (c,e) linearly and (d,f) circularly polarized excitation light.

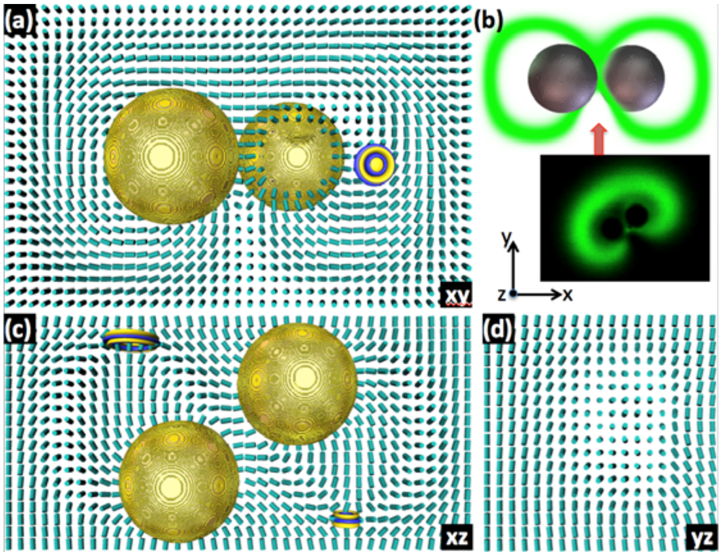

Fig. 5. Computer-simulated director configurations arising from self-assembly of colloidal elastic dipoles induced by spheres with perpendicular surface anchoring.

The spatial patterns of $\mathbf{n}(\mathbf{r})$ are depicted using cylinders and the small defect loops are shown using the bend - splay visualization [39]. (a,c,d) Computer simulated $\mathbf{n}(\mathbf{r})$ of self-assembled colloidal dimers as depicted (a) in the in-plane x-y cross-section in the cell midplane and (c,d) vertical cross-sections in two perpendicular (c) xz- and (d) yz-planes planes according to the coordinate system shown in (b). (b) The corresponding in-plane computer-simulated 3PEF-PM image for circularly polarized excitation light and $\mathbf{n}(\mathbf{r})$ shown in (a); the inset shows the corresponding experimental image. Note that the induced bulk point/ring defects of a particle dimer shown in (c) shift away from vertical axes passing through the particle's centers.

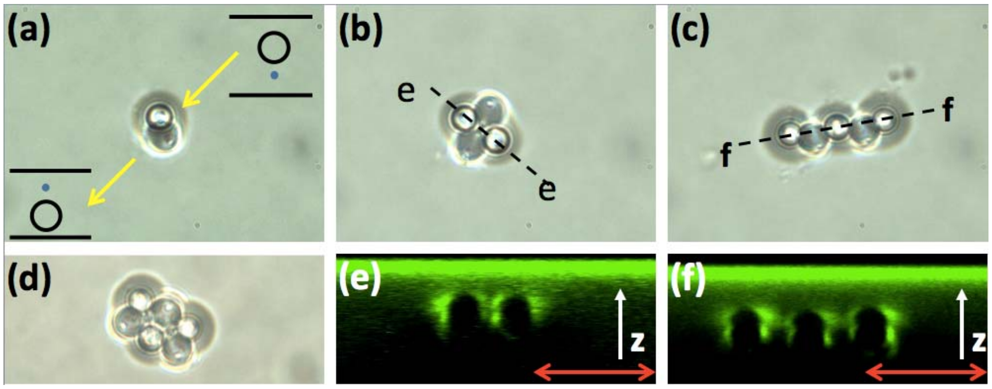

Fig. 6. Multi-particle assemblies of elastic dipoles in a cell of thickness of $d \approx 15 \mu m$ filled with a CNLCs of pitch $p \approx 20$ µm prepared by doping a chiral additive S-811 in E-31 nematic host. (a-d) Brightfield optical micrographs showing typical examples of self-assembly of anti-parallel elastic dipoles into (a) dimers, (b) tetramers, (c) pentamers, and (d) hexamers. The insets in (a) show relative locations of the 4 µm silica microspheres and the particle-induced point/ring defects, which determine the orientations of elastic dipoles. (e,f) 3PEF-PM vertical cross-sectional images, which were obtained along lines marked on (b,c), showing the details of the assembly of defects and particles obtained for linear polarizations of light having directions depicted by red arrows.

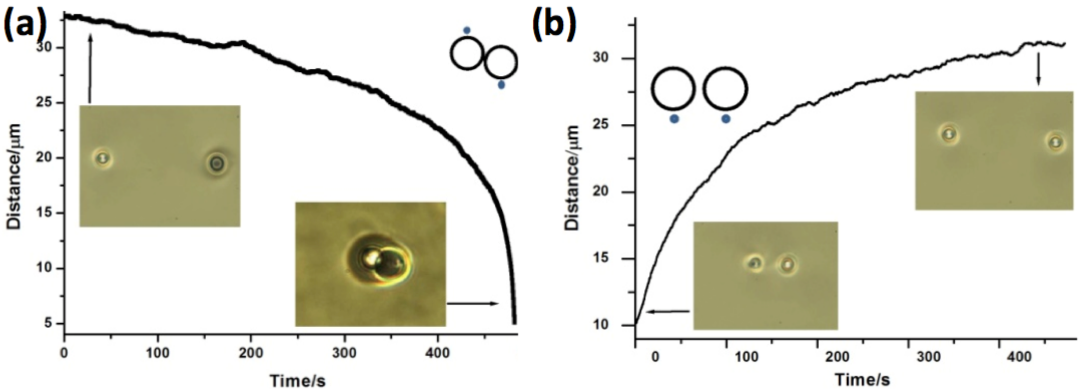

Fig. 7. Colloidal pair interactions. (a,b) Center-to-center separation versus time between two (a) anti-parallel and (b) parallel elastic dipoles probed using videomicroscopy when they are released by laser tweezers. Insets in (a) and (b) show brightfield optical micrographs taken at the corresponding initial and final center-to-center distances as well as schematically depict orientations of the elastic dipoles. The interactions were probed for 4µm silica spheres in a cell of thickness *d*≈15µm containing a CNLC with pitch *p*≈20 µm prepared by doping a nematic host E-31with a chiral additive S-811.

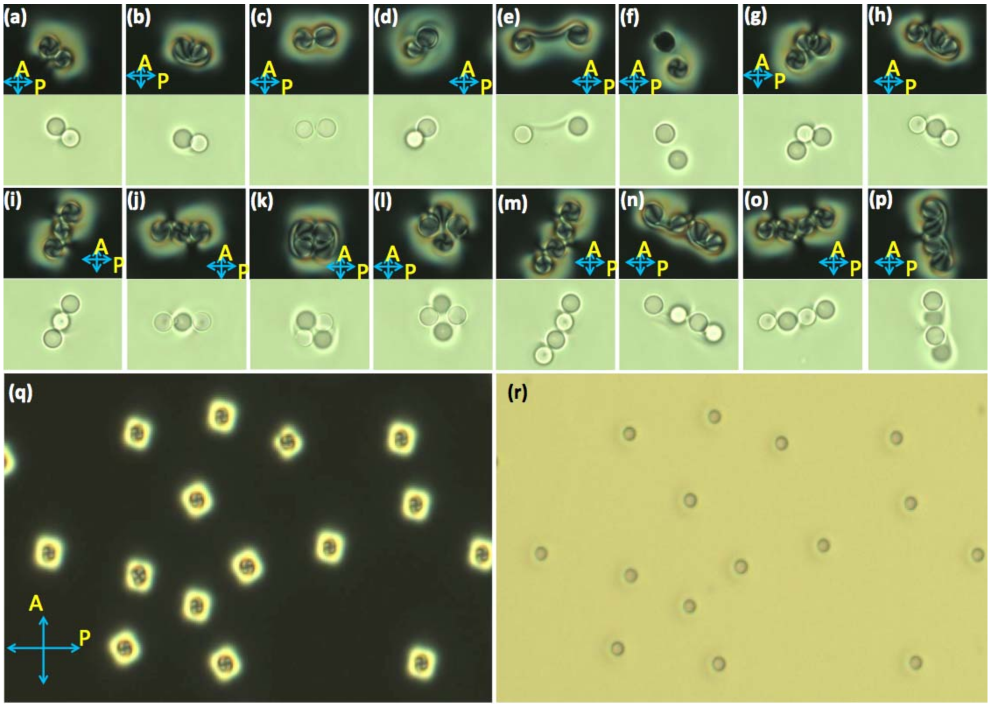

Fig. 8. Diversity of field and defect configurations of colloidal self-assemblies due to plastic particles of diameter ≈6 µm dispersed in CNLCs of pitch 10.5µm prepared by doping S-811 chiral additive to AMLC-0010 nematic host filled in a cell of thickness

d≈10µm: (a-f) dimers, (g-j) trimers, (k-p) tetramers; the particles and structures are imaged using polarizing optical microscopy (top images) and brightfield optical microscopy (bottom images). (q) polarizing and (r) brightfield optical micrographs of 6µm spacers surrounded by looped double-twist-cylinder solitons in an unwound homeotropic CNLC cell. The orientations of crossed polarizer (P) and analyzer (A) are shown using blue double arrows.

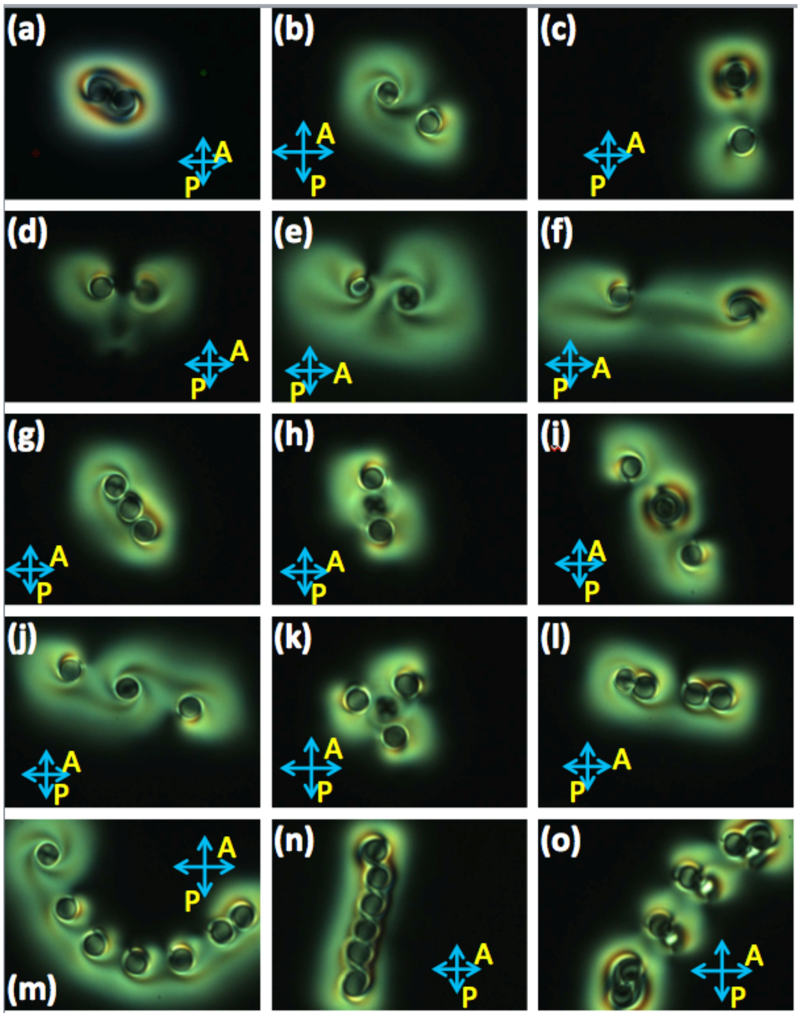

Fig. 9. (a-o) Polarizing optical micrographs of multi-particle assemblies of elastic dipoles with twisted solitons induced by 4µm silica microspheres in a cell of thickness diameter ≈10µm filled with a CNLCs of pitch 10.5µm prepared by doping a chiral additive S-811 in AMLC-0010 nematic host. The orientations of crossed polarizer (P) and analyzer (A) are shown using blue double arrows.

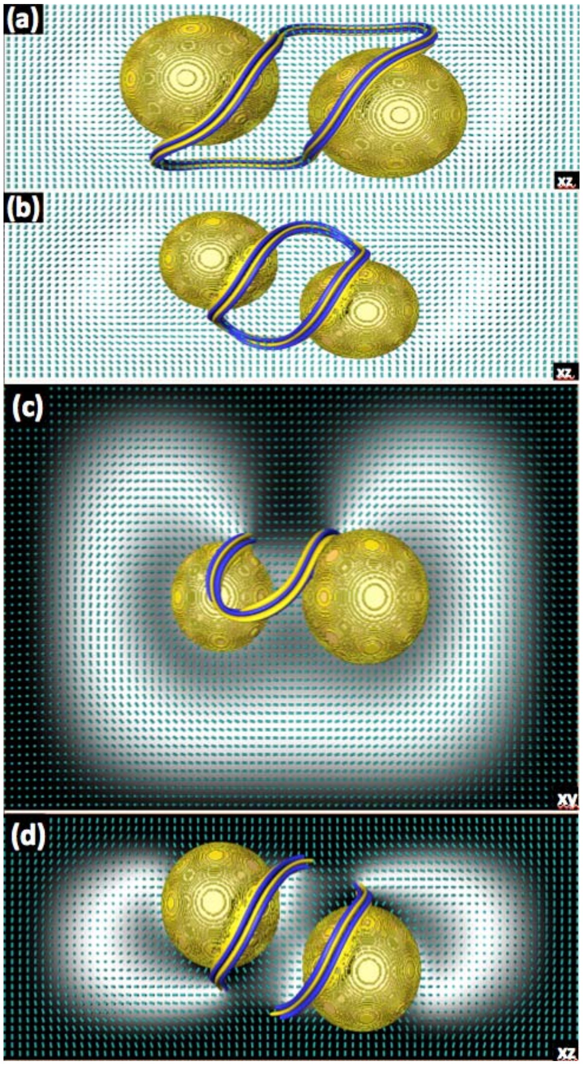

Fig. 10. Computer-simulated **n**(**r**) and 3PEF-PM textures around colloidal dimers formed by spheres with perpendicular surface anchoring and inducing both solitonic nonsingular and singular defects. (a,b) Simulated **n**(**r**) and defects of colloidal dimers depicted in vertical cross-sections passing through the sphere centers. Note that the particles are interspaced by two different closed loops of half-integer disclinations and also surrounded by nonsingular director twist distortions around them. The spatial patterns of **n**(**r**) are depicted using cylinders. (c,d) 3PEF-PM textures (shown as gray-scale intensity patterns) superimposed with **n**(**r**) depicted using cylinders for (c) in-plane and (d) vertical cross-sections of the structure shown in (b). Dislination lines are presented by iso-surfaces of the splay and bent deformations exposing their three-fold symmetry [39].

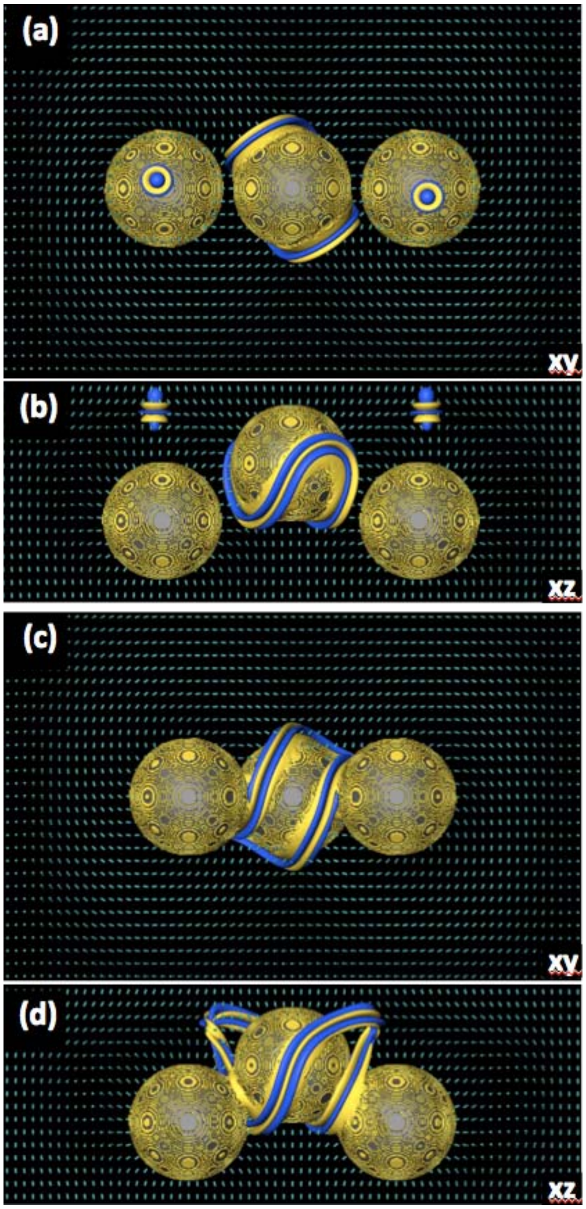

Fig. 11. Computer-simulated **n**(**r**) around colloidal trimers formed by spheres with perpendicular surface anchoring and inducing both solitonic nonsingular and singular defects. (a-d) Simulated **n**(**r**) and defects for two different structures depicted in the (a,c) in-plane cross-section corresponding to the cell midplane and (b,d) vertical cross-sections passing through the sphere centers. Note that the particles are interspaced by closed loops of singular defect lines and also surrounded by nonsingular director twist distortions around them. The spatial patterns of **n**(**r**) are depicted using cylinders and the defect lines are shown using the bend-splay visualization [39].

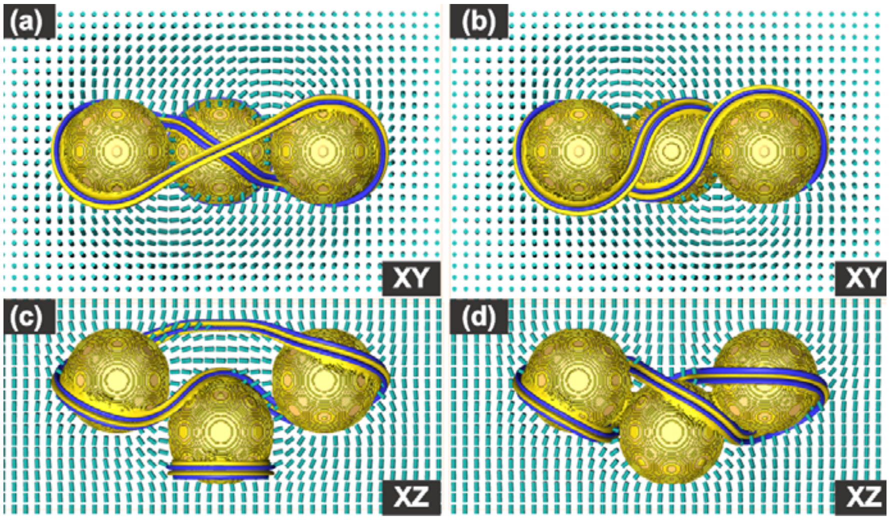

Fig. 12. Computer-simulated $\mathbf{n}(\mathbf{r})$ around colloidal trimers formed by spheres with perpendicular surface anchoring and inducing single or multiple closed defect loops. (a,b) All three particles are entangled by a single defect loop, as seen in the (a) in-plane and (b) vertical cross-section of the sample. (c,d) Two particles are entangled by a single defect loop and one particle is inducing a separate defect loop next to it, as seen in the (c) in-plane and (d) vertical cross-section of the sample. The spatial patterns of $\mathbf{n}(\mathbf{r})$ are depicted using cylinders. The spatial patterns of $\mathbf{n}(\mathbf{r})$ are depicted using cylinders and the defect lines are shown using the bend-splay visualization [39].